Journal of Nuclear Materials 462 (2015) 304–309

Contents lists available at ScienceDirect

Journal of Nuclear Materials

journal homepage: www.elsevier.com/locate/jnucmat

EELS and atom probe tomography study of the evolution of the metal/oxide interface during zirconium alloy oxidation

Benoit de Gabory [a], Yan Dong [b,*], Arthur T. Motta [a], Emmanuelle A. Marquis [b]

[a] Department of Mechanical and Nuclear Engineering, Penn State University, University Park, PA 16802, USA
[b] Department of Materials Science and Engineering, University of Michigan, Ann Arbor, MI 48109, USA

ARTICLE INFO

Article history:
Received 24 November 2014
Accepted 21 March 2015
Available online 1 April 2015

ABSTRACT

In an effort to understand the mechanisms resulting in the variations of corrosion rate observed throughout corrosion including at the first kinetic transition when the oxide temporarily loses its protective character, the oxide/metal interfaces of autoclave corroded Zircaloy-4 and ZIRLO™ before and after the transition are characterized using electron energy loss spectroscopy and atom probe tomography. The results reveal a complex structure of different phases at different stages of corrosion. The oxide/metal interface exhibits an intermediate layer, with an oxygen content between 45 and 55 O at.% and a suboxide layer corresponding to an oxygen-saturated solid solution in the metal matrix side (~30 O at.%). Local variations are observed in the width of these characteristic structural features, especially near the transition. Good agreement on the layers present as well as their order, composition, and width was seen with the two techniques.

1. Introduction

Zirconium-based alloys have been widely used in the nuclear industry for the past sixty years because of their good mechanical behavior, resistance to corrosion, and low thermal neutron absorption cross-section [1]. However, waterside corrosion and associated hydrogen pickup limit the use of zirconium alloys as fuel cladding in longer cycles and harsher conditions [2]. For a specific alloy, the corrosion rate evolves during the corrosion process, most notably when the oxide temporarily loses its protective character (oxide transition). The different corrosion rates observed in different alloys are thought to be related to the microstructure of the oxide layers formed in these alloys [3,4]. In addition, extensive work has been performed to characterize the microstructures of oxide layers before and after transition, including crystal structure, texture, grain size and morphology, porosity, and cracking [5–12].

Whereas the usual approximation made is that all the oxygen ingress results in the formation of ZrO_2, this is not strictly true: the region ahead of the advancing oxide front has been reported to show a complex microstructure with a variety of oxide phases exhibiting lower oxygen content than 66 at.% [13–16]. Particularly studies of the oxide/metal interface demonstrated by both electron energy loss spectroscopy (EELS) and atom probe tomography (APT) that one of the lower stoichiometry oxide phases is equiatomic suboxide ZrO [17–20], which is only present in pre-transition alloys and disappears briefly after transition and reforms as the oxidation rate slows down [21,22]. More recent works using transmission backscattered electron diffraction suggested that the ZrO phase has a hexagonal structure [22,23], in agreement with earlier atomistic predictions [24]. Other than the ZrO phase, other oxygen-rich phases were also reported, including ω-Zr [13], Zr_3O [10,14,25,26] and other oxygen ordered phases [17,18,20,21]. Since the thickness of these intermediate layers seem to inversely correlate with the oxidation kinetics [22,26], it is important to understand the evolution of these oxide phases.

This study presents results from both EELS and APT analyses on oxide layers formed on Zircaloy-4 and ZIRLO that were archived before and after the first kinetic transition. Both techniques allow for the characterization of the oxygen content profile across the oxide/metal interface. The structures of oxide phases present at the oxide/metal interface were elucidated by a combination of EELS analyses and transmission electron microscopy (TEM) observations. More detailed analyses of the composition and morphology of each oxide layer were obtained from the APT measurements. Results are discussed in light of the existing literature on similar alloys.

2. Experimental procedures

Zircaloy-4 and ZIRLO™ recrystallized sheet samples were autoclave-corroded in 360 °C water at saturation pressure at Westinghouse as described in [10]. The Zircaloy-4 composition is

---

* Corresponding author. Tel.: +1 (734) 546 8494.
E-mail address: yand@umich.edu (Y. Dong).

http://dx.doi.org/10.1016/j.jnucmat.2015.03.043
0022-3115/

Zr–1.45Sn–0.2Fe–0.1Cr (in weight percent). The composition of ZIRLO™ is Zr–1.0Sn–1.0Nb–0.1Fe (wt.%). The processing conditions for these alloys can also be found in [10].

The oxidation kinetics was evaluated by measuring the weight gain as a function of exposure time, as shown in Fig. 1. A periodic corrosion behavior that is characteristic of the corrosion of Zr alloys is observed for both alloys. Coupon samples were archived at different corrosion times for examination; specifically, three samples were selected from before and after the first oxide transition for each alloy, at the times indicated by the arrows in Fig. 1. The exposure time and calculated oxide thickness (determined from weight gain data) for each sample are indicated in Table 1.

Electron-transparent TEM foils and needle-shaped APT samples were both prepared through standard lift-out methods using focused ion beam (FIB) milling [27,28] using a FEI Quanta 3D 200 and a FEI Helios 650 Nanolab instruments, both operated at 30 keV, with currents between 30 pA and 7.0 nA. The APT needles were analyzed using a CAMECA LEAP-4000XHR operated in a laser pulsing mode with 200 kHz pulse repetition rate and 70–100 pJ laser energy. The temperature of the specimens was maintained at 50 K while the standing voltage was varied automatically to maintain a detection rate of 0.005 ion/pulse. Data was reconstructed and analyzed using the reconstruction software, IVAS 3.6.6. The default value of *k* factor (3.3), image compression factor (1.65) and evaporation field of Zr (28 V/nm) were selected for reconstruction.

A JEOL 2010F Scanning Transmission Electron Microscope (STEM) operated at 200 keV and equipped with a Gatan GIF spectrometer for EELS measurements was used for TEM examination. The oxygen concentration profiles across the oxide/metal interfaces were obtained by performing EELS scans, using a probe size of 1.0 nm, steps of 1.5 nm, a camera length of 8 cm and an aperture of 2 mm. The EELS edges of interest for our study are the Zr M4,5-edge at 180 eV and the O K-edge at 530 eV. The spectra were analyzed using the Cornell Spectrum Imager [29]. An exponential fit was used to estimate the background level and the edges were integrated over an energy range of 50 eV, following background subtraction. From the integrated area, the atomic composition was calculated from empirical *K*-factors obtained from a ZrO_2 standard.

3. Results

3.1. Pre-transition Zircaloy-4 samples

3.1.1. 60 days exposure (sample 1)

At the selected pre-transition time, a sequence of oxide phases is observed on sample 1 as illustrated in Fig. 2. The surface layer of ZrO_2 – shown on the left hand side – turns into an intermediate sub-oxide layer about 30–50 nm wide at the oxide/metal interface. The EELS line scan and the APT reconstruction and concentration profile indicate an approximate oxygen concentration of 48–50 at.%, which is consistent with the stoichiometry of the ZrO phase. Within this layer, we note two regions: slightly over- and slightly under-stoichiometric ZrO (denoted as ZrO_{1+x} and ZrO_{1-x}) as reported previously [18]. Below the ZrO layer, a gradual decrease in the oxygen concentration from about 37 at.% O down to 20 at.% over 150–200 nm is observed by EELS while a constant concentration of 30 at.% O over about 130 nm is measured by APT, which also shows an additional concentration steep gradient from 30 at.% down to less than 5 at.% O in the metal region. The concentration of 30% O corresponds to the oxygen saturation in Zr metal, the corresponding region in the APT data is interpreted as an ordered Zr_2O phase or sometimes also referred to as $Zr(O)_{sat}$ [18]. The width of the $Zr(O)_{sat}$ layer would reduce to almost zero if the line profile was taken 20 nm to the right in Fig. 2(b). This is in good agreement with TEM observations, in which the width of the ZrO layer was seen to be highly variable, sometimes present and sometimes not [6]. The absence of a concentration plateau in the EELS profile could be caused by the oxide/metal interface not being parallel to the electron beam.

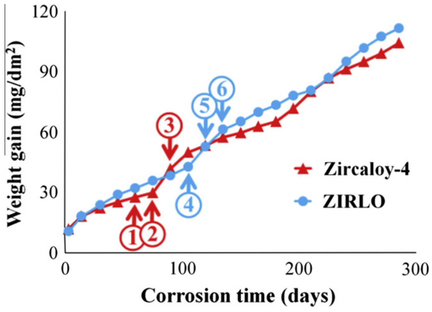

Fig. 1. Corrosion weight gain versus exposure time in 360 °C pure water for ZIRLO and Zircaloy-4. The studied samples are indicated by arrows and numbered.

Table 1
Exposure time, measured corrosion weight gain, and calculated oxide thickness for the ZIRLO™ and Zircaloy-4 samples studied.

		Sample number	Exposure time (days)	Weight gain (mg/dm^2)	Calculated oxide thickness (μm)
Zircaloy-4	Pre-transition	1	60	27.7	1.9
		2	75	29.8	2.1
	Post-1st transition	3	90	41.7	2.8
ZIRLO™	Pre-transition	4	105	42.3	2.9
	Post-1st transition	5	120	52.7	3.6
		6	135	61.2	4.2

3.1.2. 75 days exposure (sample 2)

The same observations made for sample 1 were made on the Zircaloy-4 sample oxidized for 75 days, and archived just before the first kinetic transition (sample 2). Fig. 3(a) shows the EELS line scan profile in which the O concentration fluctuates around 55 at.% right after the plateau of ZrO_2, followed by a slow decrease from 45 to 30 at.%. These fluctuations were probably due to the coexistence of ZrO and $Zr(O)_{sat}$ through the thickness of the TEM sample. According to the EELS profile, the combined thickness of ZrO and $Zr(O)_{sat}$ is larger than 300 nm. The ZrO and $Zr(O)_{sat}$ layers are also observed by APT (Fig. 3(b) and (c)). The interface between the ZrO_2 oxide and ZrO is relatively flat, while the interface between ZrO and $Zr(O)_{sat}$ is wavy, showing broad semi-elliptical regions of ZrO advancing into $Zr(O)_{sat}$ (Fig. 3(b)).

3.2. Post-transition Zircaloy-4 after 90 days exposure (sample 3)

In the post-transition sample (sample 3), no ZrO phase could be observed by EELS (Fig. 4(a)) and the APT concentration profile reveals a ZrO_{1+x} layer less than 5 nm thick below the ZrO_2 oxide layer (Fig. 4(c)). Below the ZrO_{1+x} layer, a concentration plateau of $Zr(O)_{sat}$ is observed 70–95 nm away from the ZrO_2 interface. It is possible that Zr_3O, one of the ordered phases of Zr(O) solid solution, is also present considering the slight lower oxygen level (around 25%) at the 105–125 nm of the ZrO_2 interface in (Fig. 4(a)). The oxygen concentration then abruptly decreases to less than 5 at.% O (Fig. 4(c)). The EELS line scan profile suggests a 20 nm thick layer containing around 40% O next to ZrO_2 oxide

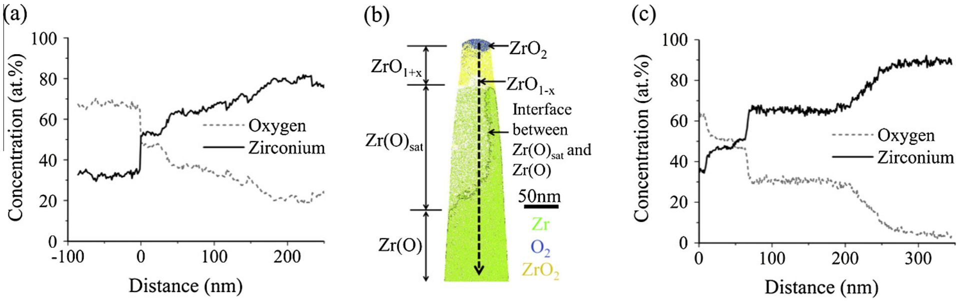

Fig. 2. Zircaloy-4 pre-transition oxide region (sample 1): (a) composition as a function of distance to the oxide/metal interface as measured by EELS; (b) 10 nm slice from an APT reconstruction showing the presence of different oxide phases; and (c) concentration profile from APT taken along the arrow indicated in (b).

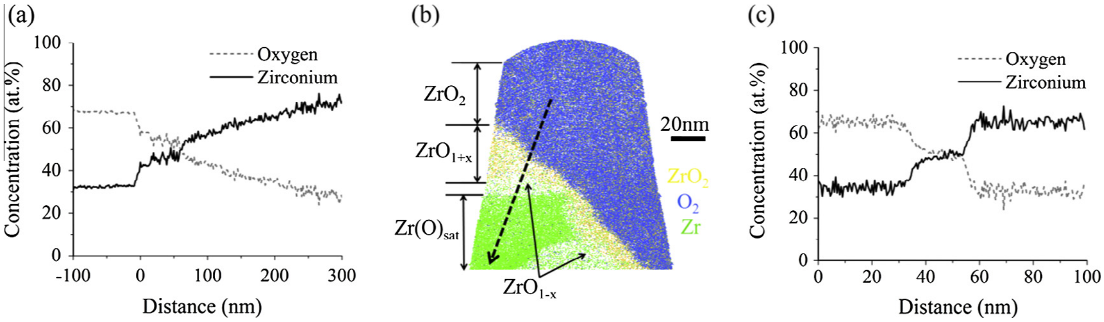

Fig. 3. Zircaloy-4 pre-transition oxide region (sample 2): (a) composition as a function of distance to the oxide/metal interface as measured by EELS; (b) 10 nm slice from an APT reconstruction showing the presence of different oxide phases; and (c) concentration profile from APT taken along the arrow indicated in (b).

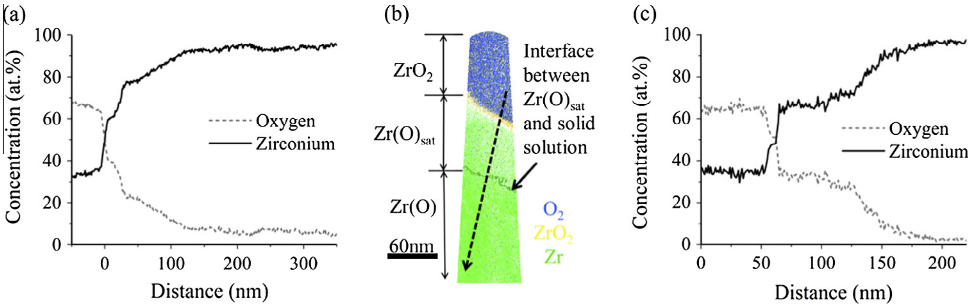

Fig. 4. Zircaloy-4 post-transition oxide region (sample 3): (a) composition as a function of distance to the oxide/metal interface as measured by EELS; (b) 10 nm slice from an APT reconstruction showing the presence of different oxide phases; and (c) concentration profile from APT taken along the arrow indicated in (b).

(Fig. 4(a)). Since the measured O concentration is intermediate between that of ZrO and $Zr(O)_{sat}$, it is interpreted as the result of the presence of both phases through the thickness of the TEM sample.

3.3. Pre-transition ZIRLO sample after 105 days exposure (sample 4)

The phase sequence observed in pre-transition ZIRLO sample (sample 4) is similar to that in pre-transition Zircaloy-4 samples 1 and 2. A gradual decrease in the O concentration from about 46% O down to 30% O is observed in EELS profile, having small plateau formed on each side (Fig. 5(a)). This region extends for over 200 nm and may correspond to ZrO and $Zr(O)_{sat}$ layers. A sharp interface between ZrO and $Zr(O)_{sat}$ is not observed possibly due to interface not being parallel to the electron beam or sample thickness variation. ZrO and $Zr(O)_{sat}$ layers can be differentiated in the APT line profile as a thin layer (5–10 nm) having around 52% O and a O concentration plateau containing around 30% O (Fig. 5(c)). The APT dataset also captures a small portion of the ZrO_{1-x} phase, extending more than 50 nm into the metal (Fig. 5(b)). According to the APT analysis, the combined thickness of ZrO and $Zr(O)_{sat}$ is about 150–200 nm, which is in good agreement with the EELS measurement.

3.4. Post-transition ZIRLO samples

3.4.1. 120 days exposure (sample 5) and 135 days exposure (sample 6)

In both post-transition ZIRLO samples, layers are arranged differently along the interface. A gradual decrease from around 55% O down to 47% O over 30 nm is observed from the EELS line scan (Fig. 6(a)) and could indicate the presence of the ZrO phase, which is more evident in the APT data where a ZrO_{1-x} finger grows into $Zr(O)_{sat}$ phase (Fig. 6(b)). The ZrO finger extends about 50 nm into the $Zr(O)_{sat}$ layer. At a location away from the ZrO_{1-x} finger, a ZrO_{1+x} layer thinner than 20 nm is observed (Fig. 6(b)).

At a different locations along the interfaces in samples 5 and 6, the EELS profiles show a decrease in O concentration from ~40 at.% down to 25 at.%, over 50–100 nm with no indication of the ZrO

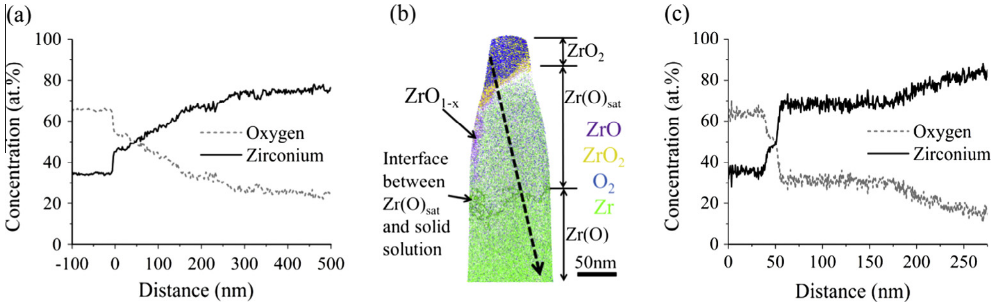

Fig. 5. ZIRLO pre-transition oxide region (sample 4): (a) composition as a function of distance to the oxide/metal interface as measured by EELS; (b) 10 nm slice from an APT reconstruction showing the presence of different oxide phases; and (c) concentration profile from APT taken along the black dashed arrow indicated in (b).

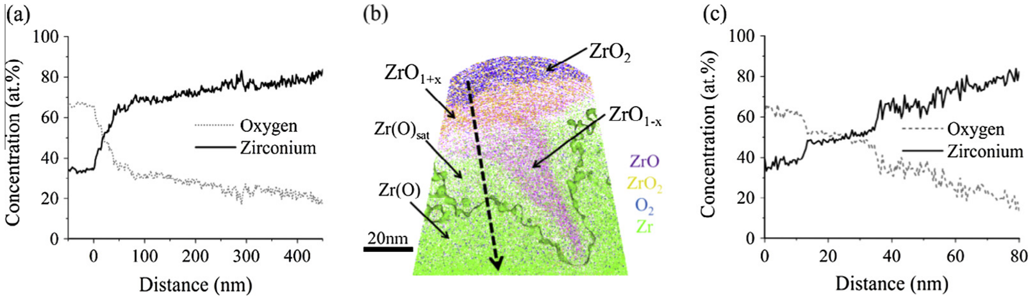

Fig. 6. ZIRLO post-transition oxide region (sample 5): (a) composition as a function of distance to the oxide/metal interface as measured by EELS; (b) 10 nm slice from an APT reconstruction showing the presence of different oxide phases; and (c) concentration profile from APT taken along the black dashed arrow indicated in (b).

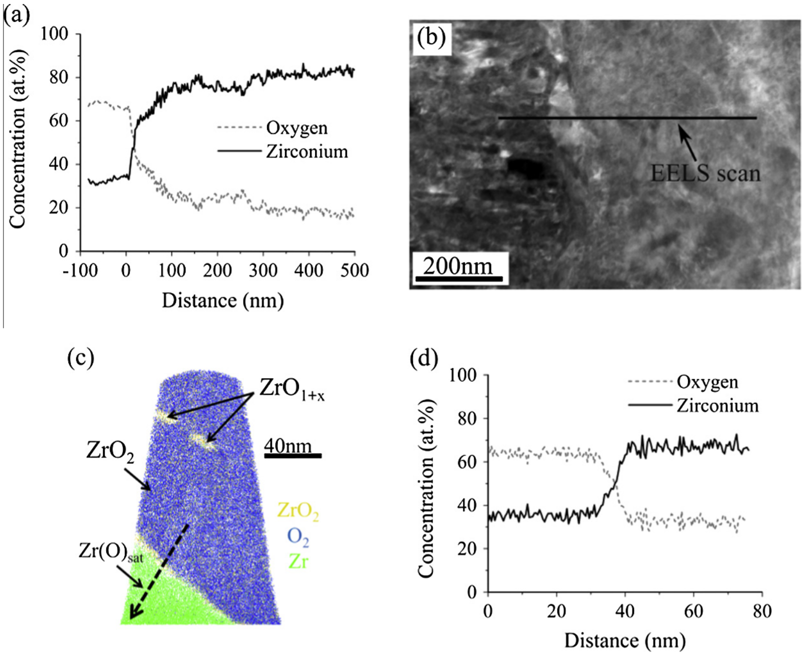

Fig. 7. ZIRLO post-transition oxide region (sample 5): (a) composition as a function of distance to the oxide/metal interface as measured by EELS; (b) HAADF image showing where EELS line scan was performed; (c) 10 nm slice from an APT reconstruction showing the presence of different oxide phases; and (d) concentration profile from APT taken along the black dashed arrow indicated in (c).

phase (Figs. 7(a) and 8). This region is likely the $Zr(O)_{sat}$ phase, which is also visible in the HAADF image (Fig. 7(b)) as the bright grain next to the ZrO_2 oxide. The absence of a ZrO layer at the interface is also observed by APT (Fig. 7(c) and (d)). The APT reconstruction also shows the existence of low-oxygen regions in the oxide (Fig. 7(c)).

4. Discussion

Although the oxide/metal interface of Zr alloys has been the subject of much research [13,14,21], its morphology is not yet fully characterized. TEM imaging, APT analysis, and EELS oxygen content profiles show a variety of structures and diffusion layers

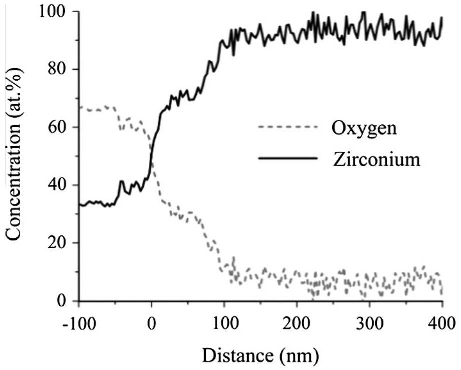

Fig. 8. ZIRLO post-transition oxide region (sample 6): composition as a function of distance to the oxide/metal interface as measured by EELS.

present at the oxide/metal interface, with local variations in the arrangement and width of these layers.

In a previous TEM study [6], through imaging and tilting, an intermediate layer was clearly identified between the metal and the oxide, with diffraction patterns corresponding to a ZrO cubic phase. In order to confirm and complete these TEM observations, the present work focused on the evolution of the oxygen content across the oxide/metal interface.

The evolution of the oxygen-containing phases is illustrated in Fig. 9. For the pre-transition samples in both alloys, the sub-oxides are generally of variable thicknesses and do not form continuous layers. The thin layer of ZrO observed by both EELS and APT varies in thickness from 0 to over 80 nm with finger like morphologies. We note that the two different layers identified within the ZrO phase by APT (ZrO_{1+x} and ZrO_{1-x}) could be an artifact from field-induced diffusion during data collection as sometimes observed during the evaporation of oxide/metal interfaces [30]. The $Zr(O)_{sat}$ layer is generally thicker (150–200 nm wide). However variations of the thickness of this layer were observed showing that this layer is not continuous along the oxide/metal interface. After transition, the ZrO layer has largely disappeared. Small ZrO fingers were occasionally observed in post-transition ZIRLO sample (120 days) but none was found in another post-transition ZIRLO sample (135 days) and post-transition Zircaloy-4. This difference in the presence of fingers is likely related to the rate of advance of the oxide front. When that is fast, any fingers of ZrO which serve as precursors of a $Zr(O)_{sat} \Rightarrow ZrO$ transformation are quickly consumed by the advancing front, so that right after transition the fingers are not observed.

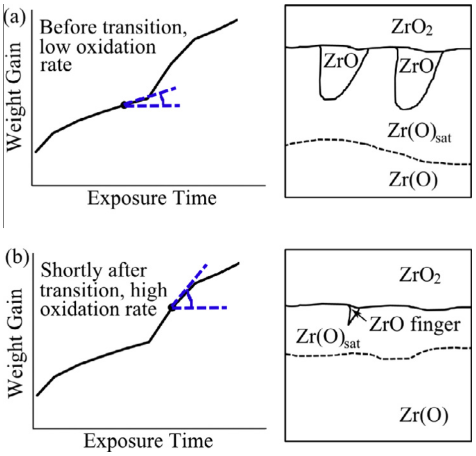

Fig. 9. Schematic illustration of oxygen containing phases present at metal/oxide interface in (a) pre-transitioned and (b) post-transitioned samples.

The present results are in broad agreement with the literature. The observed ZrO phase was reported by Ni et al. [21] using atom probe tomography and electron energy loss spectrometry (EELS) and by Hu et al. [16] and Garner et al. [23] using transmission backscattered electron diffraction. The large thickness variation of the ZrO layer agrees with Tejland's work [17,20] and adds more evidence that the transition happens locally along the interface. From the comparison between pre- and post-transition samples for both alloys, we can observe that the transition greatly affects the structure of the oxide/metal interface: the ZrO layer seems to disappear, while the $Zr(O)_{sat}$ layer seen ahead of the oxide is significantly narrower in the post-transition samples, likely because both layers are consumed by the rapid advance of the oxide layer during transition. When the oxide grows more slowly, the ZrO and $Zr(O)_{sat}$ layers start to form again.

The question remains as to how oxygen that diffuses ahead of the main oxide front and forms the intermediate phase observed affects the corrosion behavior of the alloys. Clearly the fact that some oxygen is used to form the layers, rather than forming stoichiometric ZrO_2 would cause a slight slowing down of oxide formation. However, this effect is small, since the total oxygen content in these thin layers is small compared to the overall oxygen content in the stoichiometric oxide. Also, since the sequence of phases appears to depend mostly on the stage of corrosion, it is likely that these suboxide layers are *consequences* rather than *causes* of the pre-transition corrosion behavior such that when the oxide front advances quickly the layers ahead of the oxide front are consumed. Concerning the oxide transition, as the oxide grows stresses accumulate which may be partly relieved by plastic deformation of the metal. Since the oxygen hardens the metal region next to the oxide front, the plasticity of the Zr matrix may be hampered, which would make the accommodation of stresses induced into the matrix by oxide growth (normally done by plastic deformation usually by creep) more difficult. Thus the presence of the oxygen-rich layers could accelerate stress accumulation in the oxide and thus accelerate in turn the onset of the oxide transition or possibly cause corrosion breakaway.

5. Conclusions

In this study, the oxide/metal interface has been characterized in detail using both EELS and APT, in an effort to obtain a comprehensive picture of its structure and the changes related to the oxide transition. The results presented below were obtained by a combination of various techniques, including bright field and HAADF imaging in the TEM, EELS scans, and APT analysis. A succession of phases and diffusion layers is present at the oxide/metal interface, which is clearly visible in the pre-transition oxide. From oxide into the metal these phases are:

i. An intermediate layer, associated with a cubic ZrO phase, containing between 45 and 55 at.% O.
ii. A $Zr(O)_{sat}$ oxygen-saturated suboxide layer in the metal (~30–35 at.% O in solid solution).
iii. A region in which the oxygen content is in solid solution and slowly decreases into the metal (less than 30 at.% O).

Good agreement on the thicknesses of the layers, compositions and order of the phases was seen using EELS and APT, giving greater confidence in the results as artifact that could be present in one technique would not act on the other. The width of these layers depends both on the alloy and on the stage of corrosion. In addition, local variations can be observed along the oxide/metal interface. Before transition, the ZrO layer is about 30–70 nm wide for Zircaloy-4 and about 20–90 nm wide for ZIRLO. The $Zr(O)_{sat}$ layer is about 150–200 nm wide for both alloys before transition. The interfacial regions generally disappear at the first kinetic transition in both alloys. The intermediate layer could not be observed in some samples, and was less than 5 nm wide in others. In addition, the width of the suboxide layer ($Zr(O)_{sat}$) decreases significantly (30–80 nm compared to 150–200 nm before transition). The oxygen content in α-Zr decreases faster in the post-transition samples (less than 10 O at.% 100 nm away from the oxide/metal interface) than in pre-transition samples (about 20 O at.% 400 nm away from the oxide/metal interface on EELS results). The high oxide layer advancement rates at transition consume these layers, which start to develop again as the advancement rate falls in the post transition regime. This results in steeper profiles for region iii.

Acknowledgements

The authors would like to thank Trevor Clark, Ke Wang and Josh Maier for their invaluable help and advice regarding the operation of the TEM and the FIB. This work has been made possible thanks to the variety of samples oxidized by Robert Comstock at Westinghouse, as part of the MUZIC2 program. This research was performed using funding received from the DOE Office of Nuclear Energy's Nuclear Energy University Programs under contracts # NE0000315 and # 00121106, and was partly supported by the University of Michigan College of Engineering.

References

[1] D.L. Douglass, The Metallurgy of Zirconium, International Atomic Energy Agency Supplement, Vienna, 1971.

[2] M.C. Song, K.J. Lee, A study on the generation of radioactive corrosion product at PWR for extended fuel cycle, in: International Symposium on Technologies for the Management of Radioactive Waste from Nuclear Power Plants and Back End Nuclear Fuel Cycle Activities, vol. IAEA SM 357/75, Taejon, Republic of Korea, 1999.

[3] H.-J. Beie, A. Mitwalsky, F. Garzarolli, H. Ruhmann, H.-J. Sell, Examinations of the corrosion mechanism in zirconium alloys, in: Garde, E.R. Bradly (Eds.), 10th International Symposium on Zr in the Nuclear Industry, ASTM STP 1245, Baltimore, 1993, pp. 615–643.

[4] D. Pecheur, J. Godlewski, P. Billot, J. Thomazet, Microstructure of oxide films formed during the waterside corrosion of the zircaloy cladding in lithiated environment, in: E.R. Bradely, G.P. Sabol (Eds.), 11th International Symposium on Zr in the Nuclear Industry, ASTM STP 1295, Garmisch-Partenkirchen, 1995, pp. 94–113.

[5] D. Pecheur, F. Lefebvre, A.T. Motta, C. Lemaignan, D. Charquet, Oxidation of intermetallic precipitates in Zircaloy-4: impact of irradiation, in: 10th International Symposium on Zirconium in the Nuclear Industry, ASTM STP 1245, Baltimore, 1993, pp. 687-705.

[6] B. de Gabory, A.T. Motta, Structure of Zircaloy 4 Oxides Formed during Autoclave Corrosion, in: ANS LWR Fuel Performance Meeting, Charlotte, 2013, paper #8584.

[7] D. Pecheur, F. Lefebvre, A.T. Motta, C. Lemaignan, J.-F. Wadier, J. Nucl. Mater. 189 (1992) 2318–2332.

[8] J.P. Pemsler, Electrochem. Technol. 4 (1966) 128–131.

[9] J. Godlewski, How the tetragonal zirconia is stabilized in the oxide scale that is formed on a zirconium alloy corroded at 400 C in steam, in: 10th International Symposium on Zr in the Nuclear Industry, ASTM STP 1245, Baltimore, 1993, pp. 663–686.

[10] A.T. Motta, M.J.G. Da Silva, A. Yilmazbayhan, R.J. Comstock, Z. Cai, B. Lai, Microstructural characterization of oxides formed on model Zr alloys using synchrotron radiation, in: 15th International Symposium on Zr in the Nuclear Industry, ASTM STP 1505, Sunriver, 2009, pp. 486–506.

[11] J. Lin, H. Li, J.A. Szpunar, R. Bordoni, A.M. Olmedo, M. Villegas, A.J.G. Maroto, Mater. Sci. Eng., A 381 (2004) 104–112.

[12] A. Garner, M. Preuss, P. Frankel, J. Appl. Crystallogr. 47 (2014) 575–583.

[13] P. Bossis, G. Lelievre, P. Barberis, X. Iltis, F. Lefebvre, Multi-scale characterization of the metal-oxide interface of zirconium alloys, in: 12th International Symposium on Zr in the Nuclear Industry, ASTM STP 1354, Toronto, 2000, p. 918.

[14] A. Yilmazbayhan, E. Breval, A. Motta, R. Comstock, J. Nucl. Mater. 349 (2006) 265–281.

[15] B. Hutchinson, B. Lehtinen, M. Limbach, M. Dahlback, A study of the structure and chemistry in zircaloy-2 and the resulting oxide after high temperature corrosion, 15th International Symposium on Zr in the Nuclear Industry, ASTM STP 1505, Sunriver, 2009, pp. 269–284.

[16] J. Hu, A. Garner, N. Ni, A. Gholinia, R. Nicholls, S. Lozano-Perez, P. Frankel, M. Preuss, C. Grovenor, Micron 69 (2015) 35–42.

[17] P. Tejland, Microstructure Investigation of the Oxidation Process in Zircaloy-2 – The Effect of Intermetallic Particle Size, Department of Applied Physics, Chalmers University of Technology, Sweden, 2012. Doctor of Philosophy.

[18] Y. Dong, A.T. Motta, E.A. Marquis, J. Nucl. Mater. 442 (2013) 270–281.

[19] N. Ni, S. Lozano-Perez, J. Sykes, C. Grovenor, Ultramicroscopy 111 (2011) 123–130.

[20] P. Tejland, H.-O. Andrén, G. Sundell, M. Thuvander, B. Josefsson, L. Hallstadius, M. Ivermark, M. Dahlbäck, Oxidation mechanism in Zircaloy-2-the effect of SPP size distribution, in: 17th International Symposium on Zr in the Nuclear Industry, STP 1543, West Conshohocken, 2015, pp. 373–403.

[21] N. Ni, D. Hudson, J. Wei, P. Wang, S. Lozano-Perez, G.D.W. Smith, J.M. Sykes, S.S. Yardley, K.L. Moore, S. Lyon, R. Cottis, M. Preuss, C.R.M. Grovenor, Acta Mater. 60 (2012) 7132–7149.

[22] M. Preuss, P. Frankel, S. Lozano-Perez, D. Hudson, E. Polatidis, N. Ni, J. Wei, C. English, S. Storer, K.B. Chong, M. Fitzpatrick, P. Wang, J. Smith, C. Grovenor, G. Smit, J. Sykes, B. Cottis, S. Lyon, L. Hallstadius, R.J. Comstock, A. Ambard, M. Blat-Yrieix, J. ASTM Int. 8 (2011) JAI103246.

[23] A. Garner, A. Gholinia, P. Frankel, M. Gass, I. MacLaren, M. Preuss, Acta Mater. 80 (2014) 159–171.

[24] B. Puchala, A. Van der Ven, Phys. Rev. B 88 (2013) 094108.

[25] B. de Gabory, A.T. Motta, K. Wang, J. Nucl. Mater. 456 (2015) 272–280.

[26] A. Yilmazbayhan, A.T. Motta, R.J. Comstock, G.P. Sabol, B. Lai, Z. Cai, J. Nucl. Mater. 324 (2004) 6–22.

[27] M. Schaffer, B. Schaffer, Q. Ramasse, Ultramicroscopy 114 (2012) 62–71.

[28] K. Thompson, D. Lawrence, D.J. Larson, J.D. Olson, T.F. Kelly, B. Gorman, Ultramicroscopy 107 (2007) 131–139.

[29] R. Hovden, P. Cueva, J.A. Mundy, D.A. Muller, Microsc. Today (2013).

[30] M.N. Bachhav, E.A. Marquis, On chemistry and artifact at the interface of metal oxide and metal analyzed by atom probe tomography, in: C. Instruments (Ed.) Atom probe tomography user's meeting, Madison, Wisconsin, USA, 2013, p. 41.